Proceedings of ASME Turbo Expo 2020: Turbine Technical Conference and Exposition
GT2020
June 22-26, 2020, London, England

GT2020-76152

LARGE EDDY SIMULATION OF A HIGH PRESSURE NON-PREMIXED OXY-FLAME AND ASSESSMENT OF LOW ORDER MODELS FOR THE MIXING PROCESS

J. AL AM [1],A. Degeneve[1,2],T. Schuller[1,3], R. Vicquelin[1],
[1]Laboratoire EM2C, CNRS, CentraleSupélec, Université Paris-Saclay, 3, rue Joliot Curie, 91192 Gif-sur-Yvette cedex, France
[2]Air Liquide, Centre de recherche Paris Saclay, Chemin de la Porte des Loges, B.P. 126, 78354 Les Loges en Josas, France
[3]Institut de Mécanique des Fluides de Toulouse, IMFT, Université de Toulouse, CNRS, Toulouse, France
Email: jean.al-am@student-cs.fr

ABSTRACT

Large Eddy Simulation of a non-premixed CH4/O2 flame at high pressure and featuring a moderate swirl number is presented. The simulations have been performed under the flamelet progress variable (FPV) framework. The look-up table is linked to the flow solution by means of the mixture fraction, its segregation factor and the progress variable. The length of non-premixed jet-like oxy-flames was recently seen to be well predicted by low-order models relying on the mixing process generated in the near field region close to the injector outlet as long as swirl effects are accounted for. Those mechanisms have however never been investigated at high-pressure. The motivation of this study is to assess their validity to conditions approaching industrial configurations using high fidelity numerical tools at an affordable cost. The numerical setup is first validated with experimental data on a non-reacting simulation of a coaxial jet at atmospheric pressure. A mesh refinement technique is used to match with the experimental data while reducing the CPU cost of the computations. Scaling laws for the evolution of the methane mass fraction along the centerline axis are studied and validated for non-reacting high-pressure conditions. The previously derived extension of low-order model for the flame length is then assessed with reacting large eddy simulation at high pressure oxy-combustion conditions taking into account swirl effect. Mean and instantaneous fields of mixture fraction, velocity and temperature are analyzed in the considered configuration and allow for validating the flame length model in high-pressure flames.

INTRODUCTION

Worries over climate change have led to mounting efforts on developing new technologies aiming to reduce the increased level of greenhouse emissions in the atmosphere especially carbon dioxide CO_2. Carbon capture and storage (CCS) has been under consideration as one solution to this problem, and oxy-combustion is one of the proposed methods for such techniques with a relatively low cost. It consists in replacing air, as the oxidizer, by a stream of pure oxygen. At atmospheric pressure, the overall cycle efficiency is however lowered [4] compared to conventional systems. For alternatives, pressurized oxy-combustion has been investigated where oxygen is pre-compressed in the air separation unit, which significantly reduces the compression work duty of the compressor unit leading to a better overall net efficiency [4]. Pressure increase also enables a significant size reduction for high thermal power applications [5] and an improved fuel burnout for a similar residence-time furnace operating at ambient pressure [5].

When operating a combustion facility with pure oxygen, the fuel and the oxidizer streams are often injected separately for safety reasons. Non-premixed coaxial injectors are already employed in oxy-combustion operations in the glass industry [6], in reforming burners [7] and also considered for new gas turbine technologies [8]. As O_2-enrichment increases the flame resistance to aerodynamic strain, non-premixed oxy-flames are often stabilized in the wake of the injector rim as in [9–11]. In these experimental works, the flame length was reported to be sensibly shorter than in air operations. In a recent study, Degeneve *et al.* showed that the length of oxy-flames is well predicted by

the mixing process occurring in the near-field region close to the injector outlet [11]. In this study, a model from [13, 14] is tested with O_2-enriched air and seen to account for the flame length in a large range of operating conditions.

Non-premixed oxy-flames can also feature swirl in the annular oxidizer stream. Providing a rotational motion to the flow being injected in the chamber enables high energy conversion in a small volume by improving the mixing conditions between the fuel and the oxidizer [15]. The swirl number is an annular channel is defined as: $S_2 = \int_{r_1}^{r_2} u_z u_\theta r \mathrm{d}r / (r_2 \int_{r_1}^{r_2} u_z^2 \mathrm{d}r)$, where r_1 and r_2 denotes the radius of the central and annular injection. High swirl injectors $S_2 > 0.6$ are widely used because they lead to the formation of a central recirculation zone (CRZ), which favors flame stabilization downstream the injector . When operated at a low swirl level $S_2 < 0.6$, the CRZ is cancelled and the flames remain in the jet-like regime [17, 18]. In the latter case, the flame length is reduced due to an increase in the turbulent mixing process. This feature has been added to the flame length model from [13] by taking into account the contribution of swirl in the turbulent mixing process occurring in the near-field region [11]. The scaling law for the stoichiometric flame length L_s developed with this near field approach is given as follows [11, 13]:

$$\frac{L_s}{d_1} = c_1 \left(J_{eq}^{1/2} X_{st}\right)^{-1} (1 + (kS_2)^2)^{1/2} + c_0 \qquad (1)$$

Where c_0 and c_1 are positive constant, d_1 is the central injector diameter, X_{st} the molar stoichiometric mixture fraction and $J = \rho_2/\rho_1 r_u^2$ with $r_u = u_2/u_1$ corresponds to the momentum ratio between the two streams. Change of entrainment imparted by heat release are taken into account by replacing J to J_{eq} in Eq. (1) as described in [19]. S_2 is the swirl number in the annular flow and k a constant given by $k = 2/(1 + (d_2/d_1)^2)$. Swirling the annular oxidizer stream therefore remains interesting to obtain compact flames but lying in the jet-like regime where presence of a CRZ is not desired . This configuration constitutes the target of the present study.

The reliability of this new model has however never been confronted to numerical simulations. Besides, numerical simulations of oxy-flames in the jet-like regimes are scarce [20, 21]. Numerical simulations are a good candidate to provide further information of the reacting flows than the flame length which is commonly measured in experimental studies. This constitutes a first motivation of this work. Another advantage of numerical simulations is to test these scaling laws at elevated pressure, which is experimentally challenging. For this reason, a swirling oxy-flames featuring a thermal power $\Phi = 4$ MW, at the pressure $P = 60$ bar and annular swirl $S_2 = 0.5$ is selected as a test case for the scaling law. Due to lack of experimental data for such high pressure conditions, a non-reactive methane-air numerical simulation at atmospheric pressure is first carried out for validation purpose with a similar numerical setup. Since high fidelity numerical tools are very costly in terms of CPU time regarding industrial applications, a special care is taken in this study to limit as possible the CPU cost.

The article is organized as follows. The numerical models for the turbulent reacting flow used in the following simulations are first rapidly presented, followed by a description of the computational domain adopted. Comparison of the results of the first non-reactive simulation with experimental data is then presented. An *a priori* estimation of the flame adiabatic temperature, flame length, computational time and thermal losses are carried out for the high pressure oxy-combustion simulations. Results of this latter case are then showed in three conditions: non-reactive, adiabatic and isothermal-wall simulations.

Numerical and mathematical modeling

Turbulent flow modeling

Large-eddy simulations are carried out with AVBP solver (http://www.cerfacs.fr/avbp7x/) developed at CERFACS. AVBP solves the three dimensional compressible Navier-Stokes equations on unstructured and hybrid grids witch enables the modeling of unsteady reacting flows in complex geometrical configurations. For compressible flows, a characteristic treatment for boundary conditions is required for an accurate control of wave reflections from the boundaries of the computational domain [24].

In this work, the convective terms are discretized with the Two-Step Taylor Galerkin C (TTGC) scheme [22], featuring a third order discretization in time and space. The LES subgrid model SIGMA [23] is adopted for the subgrid stress tensor and constant subgrid Prandtl and Schmidt (both equal to 0.6) numbers are considered.

Combustion modeling

The Flamelet/Progress Variable (FPV) model [25] and its non-adiabatic extension [27] are adopted in this study and incorporated in the compressible flow solver with the TTC formalism [**?**]. This non-premixed flamelet model is parametrized by: the mixture fraction Z, the segregation factor S_z, the progress variable c and a normalized enthalpy. The joint probability density function (pdf) is modeled as a β-pdf for Z and Dirac distribution for c and the enthalpy. The flamelet database is obtained from solutions of steady non-premixed flamelet equations solved numerically for different strain rates. These flamelets were carried out in this work using the Grimech 3.0 mechanism [**?**]. The progress variable c is here defined as a linear combination of species CO_2 CO and H_2O.

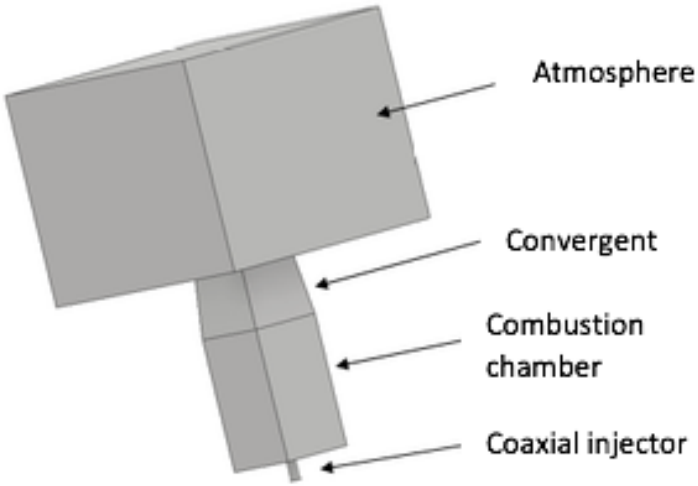

(a)

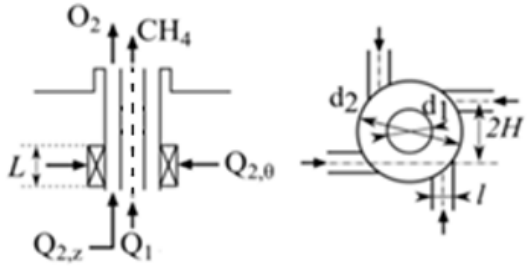

(b)

FIGURE 1: The computational domain and a schematic of the injector used for the non reacting simulation at atmospheric pressure

Radiative modeling

Thermal radiation fields are later computed using the RAINIER Monte Carlo solver [**?**] based on the Emission-based Reciprocity method [29]. Only the contributions of CO_2 and H_2O species are considered. The gas radiative properties are computed using the correlated-k model [30] based on updated parameters due to [36]. Such a combination of a Monte Carlo approach and detailed gas properties allow for an accurate description of radiative transfer.

Simulated configurations

A flame lying in the jet-like regime and featuring a moderate swirl number has been retained. The operating point has been investigated in the Oxytec combustor presented in [11, 18]. Four simulation cases have been carried out. The first simulation, $A1_{cold}$, is a non-reacting methane-air simulation at atmospheric pressure for which experimental data are available for validation purpose. The three following simulations are performed at high pressure $P = 60$ bars with a CH_4/O_2 coaxial jet configuration featuring swirl in the annular stream. The second simulation, $Ox60_{cold}$, also made in non reacting-conditions, aims at testing the scaling relation (Eq. 1) [11]. The two last simulations are performed in reacting conditions, in an adiabatic case where heat losses are discarded ($Ox60_{adiab}$) and finally by imposing the temperature at the combustor sidewalls ($Ox60_{isot}$).

TABLE 1: Boundary conditions used in the methane-air non reacting numerical simulation

Parameter	Inner injection (fuel)	Outer injection (Oxidizer)
mass flow [Kg/s]	1.8610^{-4}	3.21^{-3}
Temperature [K]	300	300
Turbulence intensity [%]	10	5
Reynolds number (diameter)	4000	12000

The computational domain is presented in Figure 1(a). The coaxial injector is sketched in Figure 1 in a longitudinal (left) and a transverse (right) cuts. The injector comprises a central tube of inner diameter $d_1 = 6$ mm which conveys the oxidizer stream, and an annular channel of outer diameter $d_2 = 20$ mm filled with an air flow for the methane-air simulation. The thickness of the burner lips is $e = 1$ mm. This injector is equipped with four tangential inlets which eventually generate a swirling flow at the inlet. Q_1 and Q_2 refer to the volume flow rates for the methane and the oxidizer streams. The injection outlet of the coaxial injector is located 5 mm above the back plane.

For the first simulation $A1_{cold}$, the oxidizer is an air mixture and the annular jet is not swirled. The tangential volume flow rate in this case is set to $Q_{2,\theta} = 0$. The combustion chamber is a parallelepiped with a 150 mm square cross section and 250 mm height equipped with four quartz windows. At the top of the chamber, a converging nozzle with an area contraction ratio of 0.8 is used to facilitate the burnt gas exhaust and to avoid ambient air entrainment inside the combustion chamber through the combustor outlet. The burned gases exhaust to the atmosphere at ambient pressure. The atmosphere is used here for numerical purpose, in order to push the outlet condition far from the computational domain.

For the three other high pressure cases ($Ox60_{cold}$, $Ox60_{adiab}$ and $Ox60_{isot}$), modifications of this configuration have been made. The CH_4/O_2 coaxial jet features an annular swirl, leading to tangential injection in the four tangential slots (Fig. 1)(b). The combustion chamber is of circular cross section. Since the operating pressure is very high $P = 60$ bars, the burnt gases are evacuated through a circular duct instead of the atmosphere outlet. The geometrical swirl number of the annular channel S_2 (Table 2) is defined by Eq. 2, assuming a solid-body rotation.

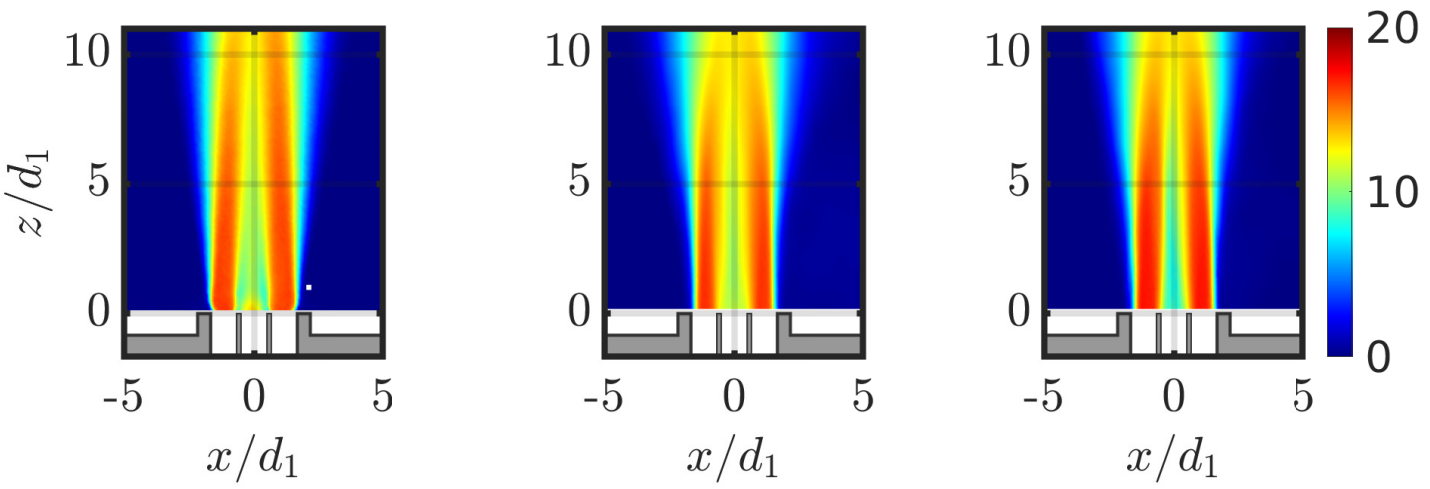

(a) Experimental data (b) MESH 1 (c) MESH 2

FIGURE 2: comparison of 2D fields of the axial velocity u_z above the injector. z is the axial dimension, x the radial dimension and d_1 the inner diameter

$$S_2 = \frac{\pi}{4}\frac{Hd_2}{NlL}\frac{1-(d_2/d_1)^4}{1+Q_{2,z}/Q_{2,\theta}} \tag{2}$$

where $H = 9$ mm is the distance separating the tangential injection channels from the burner axis, $l = 3$ mm the width and $L = 9$ mm the height of the $N = 4$ tangential injection channels (Figure 1).

Non reacting simulation

The non-reacting methane-air simulation is presented in the following. Table (1) summarizes the boundary conditions which have been used. The Reynolds number Re_1 in the central injection is calculated based on the inner diameter $Re_1 = u_1 d_1/\nu$ where ν denotes the kinetic viscosity. In the annular injection, the hydraulic diameter D_h is used with $D_h = d_2 - d_1 - e$, $e = 1$ mm being the thickness of the injector's wall.

Mesh description

The meshes used in the simulations were created using the CentaurSoft software. Tetrahedral and unstructured meshes are adopted. A refinement is applied in the mixing regions between the two flows. These regions correspond to the shear layers characterized by an intense turbulence level in the wake of the inner and outer injector rim. Two meshes M1 and M2 were generated and compared in this simulation. Two cuts above the injector are showed in Figure 3. The first mesh M1 features a relatively coarse mesh with 5 millions cells and smallest cell of $1.33.10^{-12}$ m^3. The second configuration M2, is refined with 8 millions cells with a smallest cell of $3.43.10^{-13}$ m^3. The refined mesh M2 is obtained by an automatic method of mesh refinement as proposed by Daviller *et al.* [31]. This method is based on a sensor that flag the critical regions for refinement corresponding to the shear layers. The metric proposed by [31] is the factor of dissipation of kinetic energy Φ_k defined as :

$$\Phi_k = (\mu + \mu_t)(\frac{\partial \tilde{u}_i}{\partial x_j} + \frac{\partial \tilde{u}_j}{\partial x_i})^2 \tag{3}$$

Where μ and μ_t are the molecular and turbulent viscosity respectively and $\tilde{u}_i$ is the filtered component i of the velocity in the framework of the LES approach.

.

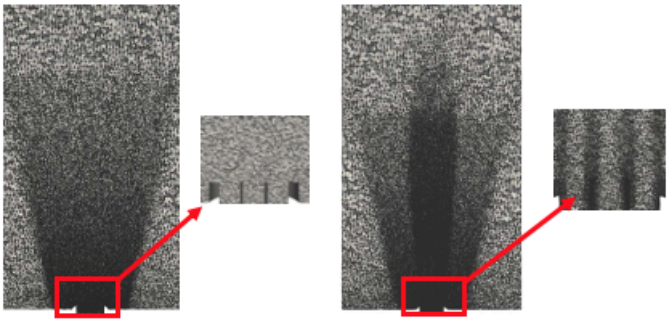

FIGURE 3: Longitudinal cuts of the mesh grids above the injector. Left: corse mesh M1. Right: refined mesh M2.

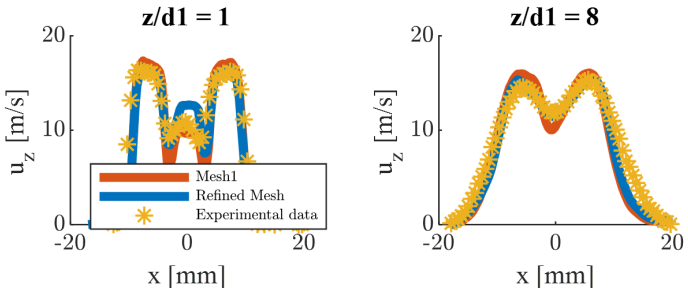

FIGURE 4: Comparison of the mean component of the axial velocity $\overline{u}_z$ profiles for different heights above the injector $z/d_1 = 1$ on the left and $z/d_1 = 8$ on the right.

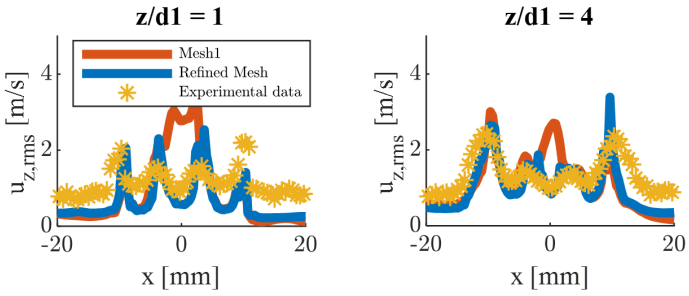

FIGURE 5: Comparison of the fluctuating component of the axial velocity $u_{z,rms}$ profiles for different heights above the injector $z/d_1 = 1$ on the left and $z/d_1 = 4$ on the right.

Comparison with experimental data

Comparison is made between the numerical simulation and the experimental data for the first simulation for the first case $A1_{cold}$. The mean component of the axial velocity is shown in Fig. 2. Velocity profiles are extracted at different heights above the injector and represented in Fig. 4 . The velocity are compared between the experimental data and those obtained numerically with the meshes M1 and M2. z denotes the axial height, x the radial dimension and d_1 the inner injector diameter. It results that the refined mesh is able to well reproduce the flow in the shear layers as well as in central flow. This good agreement is very well shown at a high distance from the injector. However, small differences may be noticed for the coarse mesh M1 especially in the mixing region between the two flows.

Figure 5 shows the profiles (for different heights above the burner) of the rms axial velocity fluctuations given by experimental data and those obtained by the numerical simulation for the two meshes. These fluctuations are proportional to the turbulent structures intensity. We can notice the good agreement whrn using the refined mesh espacially for the height ($z/d_1 > 4$). The inner shear layers (the two central pics shown in the profiles) and the outer shear layers (the two external pics shown in the profiles) are well reproduced by the refined mesh. The layers corresponding to maximal turbulent intensity are related to the mixture between the two jets (for the inner shear layer) and the mixing between the outer jet and the low velocity mixture in the chamber (for the outer shear layer). Some differences can be noticed especially in regions near the injector. In these regions, turbulence is controlled by the manner of injection. In the simulation, a homogeneous isotropic turbulence is injected witch is not the case in real experience.

Even at high distances from the injector, mesh 1 is not able to well reproduce all these turbulent properties. Thus, when comparing between the results from the two meshes, the importance of the automatic mesh refinement is observed to well predict the finest physical phenomena taking place in the mixing regions with a relatively low number of cells leading to a very reasonable computational cost for a high fidelity simulation. In fact, the two meshes have almost the same number of cells but these cells are better distributed in the refined mesh case. This method will be used for the high pressure oxy-combustion simulation.
This simulation has allowed us to validate our high fidelity large eddy simulation approach by experimental data. The same LES setup will be used for the high pressure jet-like pure oxy-flame simulation. The quality of the reacting simulation depends widely on the flow and turbulence characteristics especially in the inner and outer shear layers that are very well predicted. The dependency of the results on the mesh properties is also highlighted. The validation was done at a relatively low computational cost thanks to an automatic strategy of mesh refinement. Thus this strategy will also be used in the following high pressure reacting simulation.

High pressure oxy-combustion simulation

Preliminary calculations and combustor's design

Numerical simulations are now performed in oxy-combustion operation at elevated pressure $P = 60$ bar. As the experimental data are not available in those conditions, the operating parameters of the following cases are chosen to be representative of industrial configuration at high pressure with partial oxidation [32] or oxy-fuel gas turbine applications (ref). These parameters are assembled in Table 2. The dimensions of the injector and of the combustion chamber are chosen to simulate a small computational domain leading to a reduced computational cost of the simulation. The flame length has therefore be *a priori* adapted to the dimensions of the combustion chamber. The injecting conditions for a compact flame have been selected relying on the model given by Eq. 1. It is recalled that this model has never been tested under the investigated operating conditions, and that its validation constitute one motivation of this study. Equation 1 is first assumed to be reliable for the selected operating conditions. Its validity will then be extensively verified with the result of the numerical

simulation.

Based on eq. 1, the stoichiometric flame length L_{st} depends on the equivalent momentum flux ratio $J_{eq,sw}$ and of the mixture fraction X_{st}. This latter is fully determined by the nature of the oxidizer (pure oxygen) and the fuel (methane) $X_{st} = 0.2$. For $J_{eq,sw}$, the equivalent density ρ_{eq} is first estimated with the T_{eq}: $\rho_{eq} = 4.3$. The method described in [19, 33] is used here for the determination of the equivalent temperature and yields $T_{eq} = 5250$ K. By fixing the operational parameters (see Table 2) the square of the ratio of the inlet axial velocities u_2/u_1 depends only on the injector diameters d_1 and d_2. The outer diameter $d_2 = 20$ mm is taken equal to the one used for the previous calculation $A1_{cold}$ to conserve the same congestion. In these conditions, the flame length L_{st} only depends on the inner injector diameter d_1: $L_{st} \propto 1/d_1$. The inner diameter d_1 is set to $d_1 = 12$ mm which leads to the flame length $L_{st} = 300$ mm. All the numerical values are detailed in Table 2. The burned gases properties were computed for a methane air diffusion flame at $P = 60$ bar using the Grimech 3.0 mechanism [28]. The combustion chamber height H is be taken sufficiently larger than the flame $H = 1.7L_{st}$. In order to further reduce the computional cost of the numerical simulation, the residence time in the chamber has also been reduced by setting a moderate diameter of the combustion chamber $D = 80$ mm.

In order to predict the overall cost of the numerical simulation, the computational time is first estimated. The time step Δt of the AVBP solver is based on the acoustic time and is determined using the CFL criterion given by:

$$CFL = \frac{|u+c|_{max}\Delta t}{\Delta x_{min}} \leqslant \alpha \tag{4}$$

where α is a positive real number, u and c are approximations of the axial velocity and speed of sound respectively and Δx_{min} denotes the dimension of the smallest the cell in the mesh. Taking a CFL number of 0.7 for a physical time to be equal to 5 times of the residence time of the burnt gases in the chamber, an estimation of the overall computation time $\tau_{comput} = 55000$ CPU hours is given in table 2.

Sizing of the combustor can be completed with an *a priori* estimatation of the thermal heat losses. The overall radiative heat flux Φ^{rad} is computed with the help of the Mean Bean Length (MBL) method [34], which is an engineering method giving a rough estimate of the radiative heat transfer. Considering an equivalent gas column of length L emitting to the surrounding walls, the radiative flux yields [35]:

$$\Phi^{rad} \simeq \sigma\left(\varepsilon(L){T_g}^4 - {T_w}^4 S\right) \tag{5}$$

where T_w and T_g are the wall and gas temperature. The wall

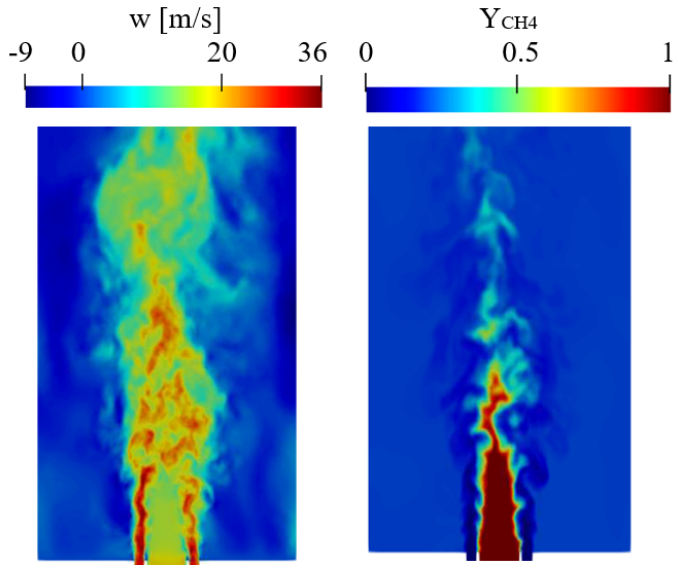

FIGURE 6: Instantaneous fields of the axial velocity $w[m/s]$ (left) and of the CH_4 mass fraction (right) above the injector (up to $z = 7d_1$).

temperature is set to $T_w = 1800K$ and the gas temperature to $T_g = 2700$ K. $\varepsilon(L)$ denotes the equivalent emissivity. For a given gas temperature, the emissivity ε_k of each component k in the medium having a molar fraction X_k is obtained as a function of the product $X_k PL$ where $P = 60$ bar is the operating pressure. In this work, these emissivities are calculated based on the work of Rivière *et al.* [36]. The Mean Beam Length Method states that a rough approximation of the equivalent gas column length is:

$$L = 3.6\frac{V}{S} \tag{6}$$

where V and S are the volume and the boundary surface of the considered medium respectively. Validity of the MBL approximation has been investigated in the literature [37, 38]. An overestimation of the radiative power from 25 to 45 % is reported on a large number of applications. Hoewever, this error remains much lower than the one obtained with other approximate techniques such as the gray gas or the optically thin approximations [37]. In this calculation, only the contributions of CO_2 and H_2O species are considered. In the present study, the MBL method leads to $\Phi = 101$ kW.

Convective heat losses are estimated using the Dittus-Boelter correlation [39] for the Nusselt number. This yields for the overall convective heat flux $\Phi = 122$ kW. It results that the total heat losses $\Phi^{rad} + \Phi^{conv}$ only constitute 6 % of the flame thermal power $P = 4$ MW. Consequently, it is reasonable to perform the following simulation $Ox60_{adiab}$ in an adiabatic condition neglecting heat losses.

TABLE 2: Operating conditions, combustor's dimensions and global properties for the high pressure oxy-combustion simulation

	Parameter	Value
Operational conditions	Operating pressure P [bar]	60
	Inlet temperature T_1 [K]	300
	Thermal power [MW]	4
	Global equivalence ratio	0.95
	Swirl number S_2	0.5
Injector Geometry	Central diameter d_1 [mm]	12
	Annular diameter d_2 [mm]	20
Chamber Geometry	Height H [mm]	500
	Section Diameter D [mm]	80
Burt gases and flame properties	Temperature T_{ad} [K]	3600
	Density ρ [Kg/m^3]	4.6
	sound speed c [m/s]	1260
	Equivalent Temperature T_{eq} [K]	5250
	Equivalent density ρ_{eq}[Kg/m^3]	4.39
	Flame length L_{st} [mm]	300
Computational time	Physical time τ [ms]	140
	Size of the smallest cell Δx [mm]	0.2
	Computational time [CPU hours]	55000
Thermal losses	Radiatif heat flux Φ^{rad} [KW]	101
	Convectif heat losses Φ^{conv} [KW]	122
	Pourcentage of heat losses [%]	6

Cold case simulation

Results for the high pressure methane-oxygen coaxial jet are first presented with the simulation $Ox60_{cold}$. The same high fidelity AVBP code, numerical schemes and turbulence models are adopted as in the atmospheric simulation $A1_{cold}$. Comparison is also made between two meshes. The first with 8.5 millions cells and the second with 16 millions cells obtained with the same automatic refinement technique as in the previous simulation.

Figure 6 depicts the instantaneous fields for the axial velocity w and the methane mass fraction Y_{CH_4} above the injector. The instantaneous turbulent structures well develop downtream the injector thanks to the LES approach. This features especially prevails in the wake of the injector central rim. It also appears that central methane stream is almost diluted at the height $z = 7d_1$. This justifies the length taken for the computational domain $H = 500$ mm.

Figure 7 shows the averaged fields of the axial velocity w, its rms fluctuations w_{rms}, the mass mixture fraction of methane and the dissipation in the kinetic energy Φ_k as expressed in eq. 3. In the axial velocity field, the contour corresponding to $\overline{w} = 0$ is also presented. Thus, the outer recirculation zones where $\overline{w}$ takes negative values are well identified. The effect of the chamber confinement on the fluid dynamics in theses zones has an important effect of the mixture composition and burnt gases flow in the re-

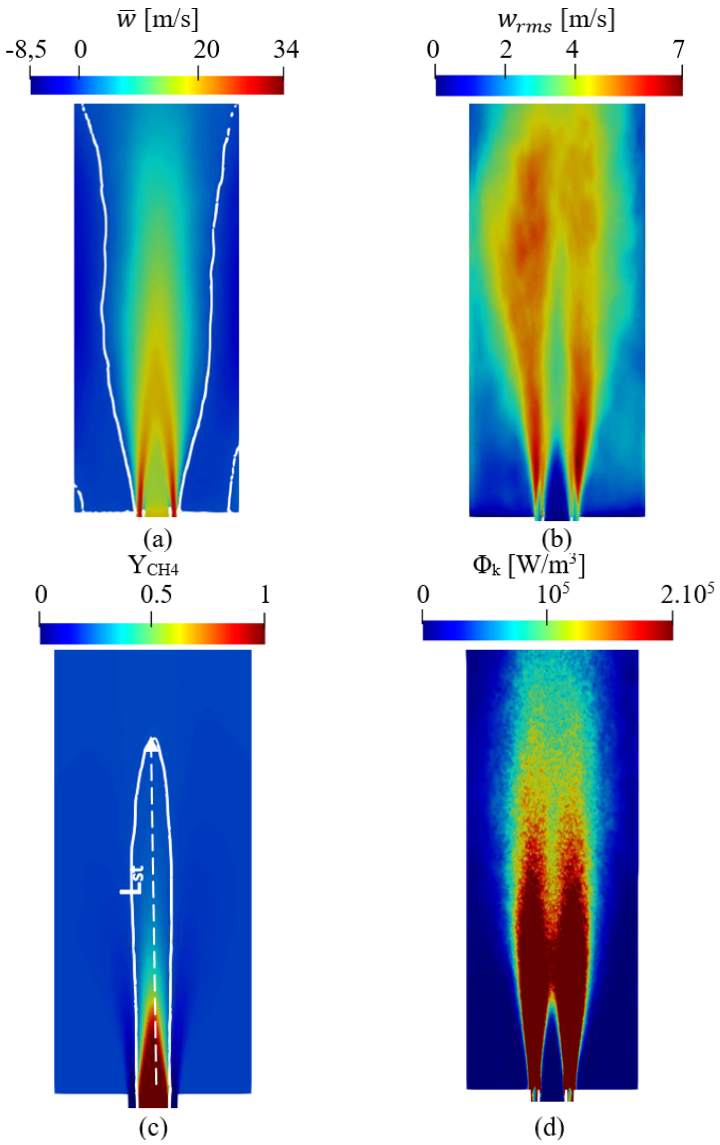

FIGURE 7: Averaged fields of the axial velocity $w[m/s]$ and the null axial velocity line is shown in white contour (a), its rms fluctuations $w_{rms}[m/s]$ (b), the methane mass fraction and the stoichiometric line is shown in white contour (c) and the factor of dissipation of kinetic energy (Φ_k) (d) above the injector (up to $z = 10d_1$)

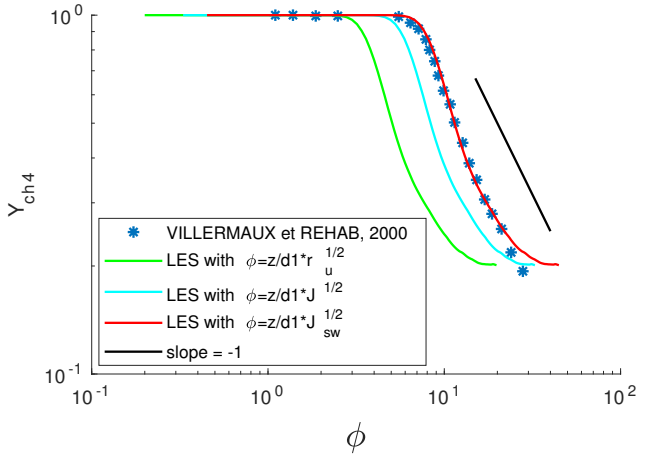

FIGURE 8: Comparison of the mass fraction profiles of the methane with an experimental scaling law developped by Villermaux and Rehab, 2000 [13]

acting case. We can also notice the absence of inner recirculation zones since the swirl number is moderate. The flame therefore well belongs to the jet-like regime conformingly with [17]. Turbulent structures intensity can be quantified through the rms fluctuations fields or the dissipation in the turbulent kinetic energy. We can clearly identify the two shear layers characterized by a maximum turbulence activity: The inner shear layer (ISL) and the outer shear layer (OSL) corresponding to the mixture regions. This justifies the choice of the dissipation of kinetic energy factor as a metric for the automatic refinement strategy. For the methane mass fraction field, the contour on witch this mass fraction is equal to its stoichiometric value ($Y_{CH_4} = Y_{CH_4,st} = 0.2$) is also showed. A parameter of interest is the stoichiometric length L_{st}. This length is proportional to the flame length in the reacting case and it can be estimated by the same model developped for the flame length and showed in Eq. 1. For that, the temperatures T_1 and $T_{2_{eq}}$ are equal to the fresh gases temperatures ($300K$ here). By doing so, we obtain an estimation of this length given by the model as: $L_{st}/d_1 = 14.3$. Measuring this quantity from the results of the LES high pressure numerical simulation, one obtains $L_{st}/d_1 = 13.9$ witch corresponds to an error of only 3%. The low order model developped for atmospheric pressure is thus very well validated at high pressure non-reacting case. This means that, even at high pressure operational conditions, mixture characteristics are still controlled by the turbulent instabilities in the shear layer between the two flows near the injector.

After validating the low order model for the stoichiometric length, a comparison between the numerical results of the evolution of the mass fraction of methane Y_{CH_4} in function of a normalized scaling height (ϕ) to a scaling law developped by Villermaux and Rehab, 2000 [13]. In this latter work, the scaling law was developped for a coaxial non swirled jet at atmospheric pressure, the two flows (water) having the same density. The Reynolds number (according to the inner diameter d_1) is of the order of 15000 and the inlet velocity of the central fluid is lower than that of the annular one ($r_u > 1$). The scaling parameter that was found in this work is $\phi = z/d_1 r_u$. For that, figure 8 shows, in a log-log scale plot, the experimental scaling law (blue dots) and the evolution of Y_{CH_4} in function of the scaling parameter $\phi = z/d_1 r_u$ (green line). The same decreasing rate (slope of -1) can be observed in the two cases. However, the two profiles don't collapse. For that, the momentum flux ration J is first introduced taking into account the density difference between the two flows in numerical simulation. By plotting the numerical evolution of methane in function of $\phi = \frac{z}{d_1} J^{1/2}$, a better representation is obtained showed by the blue curve. The remaining difference is finally attributed to the effect of the swirling motion on the turbulence intensity. As it is done for the flame length model by *et al* [11], this effect is taken into account through $J_{sw} = J(1+(kS_2)^2)^{1/2}$. Plotting methane evolution in function of this new scaling parameter $\phi = \frac{z}{d_1} J_{sw}$, one obtains the red curve. Thus, a very good agreement can be observed. On one hand, this result prove that all the parameters that were introduced can reproduce the physical phenomena in a very good manner. On the other hand, the validity domain of this scaling law is extended for high pressure conditions and a new scaling parameter is introduced allowing to take into account density difference and swirling effect on the central jet evolution.

Adiabatic hot case simulation

The same injection conditions used for the previous simulation are adopted in this reactive adiabatic simulation $Ox60_{adiab}$ where heat losses are not considered. Figure 9 shows the instanteous fields of the temperature and the mixture fraction in the combustion chamber above the injector. It can be directly observed the very high temperature obtained by this high pressure oxy-flame compared to atmospheric methane air combustion. Contours of the maximum temperature ($T = T_{max}$) and stoichiometric mixture fration $z = z_{st}$ are also presented. It can be noticed that these two contours are almost identical. witch means that the flame, in this case, can be defined either by the maximum temperature or by the stoichiometric mixture fraction. This implies that the chemical time of such a reaction is very small compared to a flow characteristic time and confirms that the reaction zone is well controlled by the mixture between the two flows for a pure oxy-flame. The large increase in pressure leads also to a reduction of the reaction chemical time. Moreover, the effect of the confinement due to combustion chamber sidewalls on the flow and the temperature field in the outer recirulation zone (ORZ) is well remarqued. The temperature in this zone is lower than the the burnt gases adiabatic temperature (around 3500 K corresponding to the

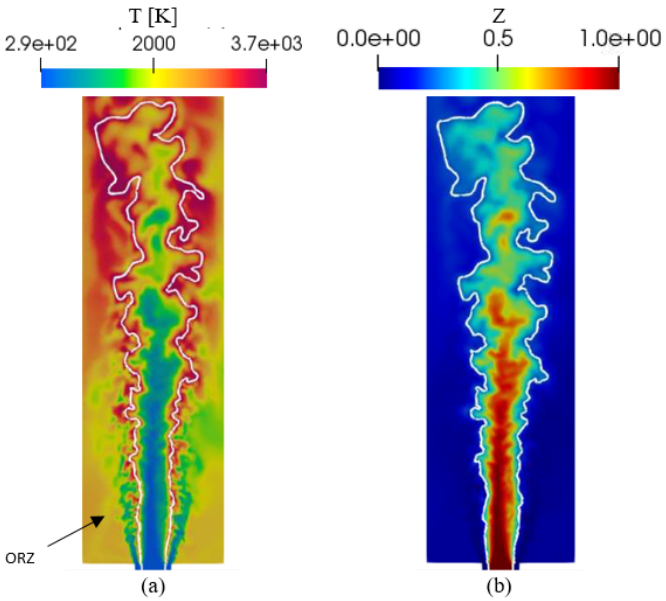

FIGURE 9: Instanteneous fields of the temperature T and the mixture fraction Z above the injector (up to $28d_1$) for the adiabatic case simulation

global equivalence ratio of 0.95). The ORZ is thus filled with a very lean mixture.

Figure 10 (a) shows the probability density function (PDF) of the flame length. Each flame length sample corresponds to the height above the injector for witch the mixture fraction is equal to its stoichiometric value for each instantaneous numerical solution. Stochastic nature of the high turbulent flow and its effect on the flame is well shown by this plot. Thanks to the LES approach, these instationarities are well reproduced. A normal fit is used to represent the flame length probability density. The estimated mean of this normal fit is 331.6 mm witch corresponds to the mean flame length ($L_{st}^{LES} = 331.6mm$) and the relative (to the mean) standard deviation is 0.012. This higher stoichiometric length compared to the previous cold case is due the thermal expansion caused by the high temperature in the chamber. Comparing this result, obtained by this high fidelity numerical simulation to the flame length estimation obtained by the law order model (Eq. 1) given in table 2 ($L_{st}^{MOD} = 300mm$), an error with respect to the numerical results of only 10 % can be noticed. This result is very satisfactory for a such law order model. Thus, for the second time, this law order model is validated and this time in a reacting high pressure oxy-combustion case. At this point, it is worth considering the scaling law developped by Villermaux and Rehab [13] for the reacting case. A scaling parameter was shown to lead to a very good agreement in the cold case is $\phi = z/d_1 J_{sw}^{1/2}$. In addition to the ratio of the inlet velocities r_u taken by [13],

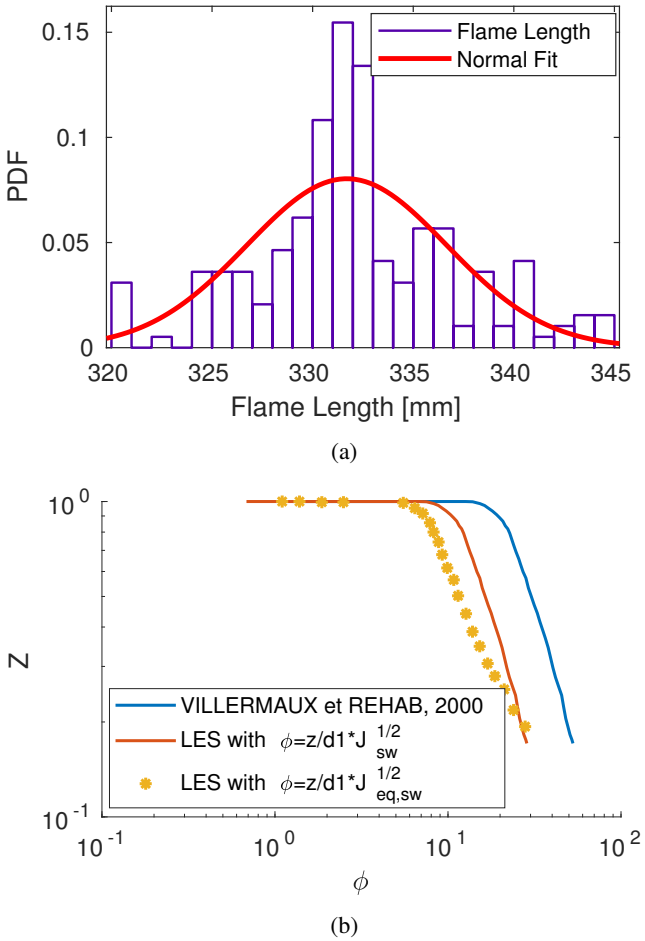

FIGURE 10: (a). Probability Density Function (PDF) of the flame length for several instantaneous solutions represented by a normal fit (b). comparison of the averaged profiles the mixture fraction obtained numerically with an experimental scaling law developped by Villermaux and Rehab [13]

this last scaling parameter takes into account the density difference between the two flows and the swirl effect on the flame structure. By plotting the numerical results of the evolution of the mixture fraction Z in function of this parameter, one obtains the blue curve in figure 10 (b), to be compared to the experimental scaling law also presented in this figure. The differences between these two curves are reffered to the thermal expension caused by the high increase of the temperature. This effect is taken by considering the equivalent density in the annular flow $\rho_{2,eq}$. Thus, the final scaling parameter will be $\phi = z/d_1 J_{eq,sw}^{1/2}$ where $J_{eq,sw} = J_{sw}\rho_{2,eq}/\rho_2$. Plotting the result of the evolution of the mixture fraction in function of this parameter, the red curve showed in figure 10 (b) is obtained. Comparing to the experimental results of the scaling law, a good agreement can be ob-

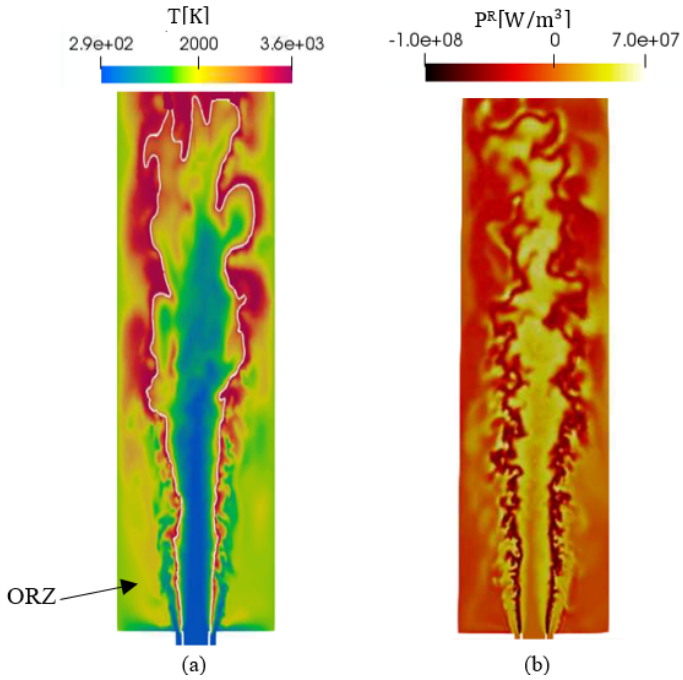

FIGURE 11: Instanteneous fields of the temperature T (a) and the radiative power P^R (b) above the injector (up to $28d_1$) and the PDF of the flame length

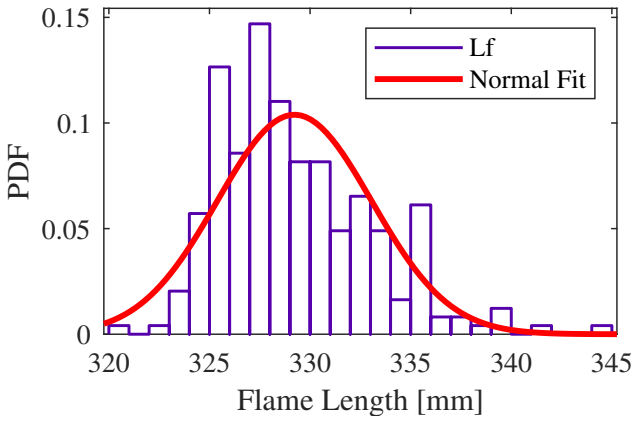

FIGURE 12: Probability Density Function (PDF) of the flame length for the iso-thermal case simulation

served showing that this model is still validated in the reacting high pressure pure oxy-combustion case. This result leads also to the conclusion that the corrective method introduced by Tacina and Dahm [19] and used by Degeneve *et al* [11] is well adapted.

Isothermal hot case simulation

The quantification of heat losses from the combustor's wall and the analysis of the effect of these losses on the temperature field and flame length constitute a crucial point in the study of any energy process. For that, the isothermal simulation case ($Ox60_{isot}$) was carried out by fixing a temperature profile on the walls (1800 k on the chamber's walls and a linear function of the radius on the combustor's base from 300 K to 1800 K). The same injection conditions used for the previous simulations are adopted here. Without taking into account radiative heat losses, figure 11 (a) shows the temperature instantaneous field and the contour corresponding to the maximal temperature above the injector in this simulation case. By comparing with the adiabatic case, convective heat losses effects can be noticed: The temperatures in the flame zone and in the outer recirculation zone (ORZ) are lower than those of the adiabatic case by about 100 and 500 K respectively. Like it has been done for the adiabatic case, the probability density function for the flame length is shown in figure 12. Using a normal fitting function a mean flame length of 328.5 mm and a relative standard deviation of 0.016 can be found. Thus, the effect of convective heat losses on the flame length are negligible (reduction of 1 %).

Finally, it is interesting to calculate the total heat losses and to compare the results to the law-order estimations given above. By integrating the wall heat flux, one obtains a total convective heat losses of $\phi^{conv,num} = 195$ KW witch is within the same order of magnitude of the previous estimation (122 KW) and constitutes 5 % of the flame thermal power (4 MW). On the other hand, the total radiative power (P^R) field above the injector is presented in figure 11 (b). High radiative emitted power regions correspond to high temperature regions and to negative total radiative power P^R. However, positive radiative power are related to high rate of reabsorbed radiative power by CO_2 and H_2O elements mostly present in the burnt gases. By integrating the total radiative power over the volume, one obtains $\phi^{rad,num} = 77$ KW to be compared to 101 KW obtained by the MBL method and to the flame thermal power (4 MW). Thus, despite the very high temperatures, the radiative losses only constitute 2 % of the overall thermal power. Emitted (ϕ^e) and reabsorbed (ϕ^a) radiative powers were also calculated leading to: $\phi^e = 628KW$ and $\phi^a = 551KW$. Thus, 88 % of the emitted power is reabsorbed by the burnt gases witch justifies the relatively law total radiative losses.

Conclusion

The validity of low order models of high-pressure non-premixed pure oxy-flame length has been assessed numerically in this work. High fidelity numerical approaches for turbulence and combustion modeling are used. Numerous large eddy simulations are performed in reacting and non-reacting conditions. Available experimental data on the mean axial velocity magni-

tude and the root mean square fluctuations are used to validate the LES numerical setup in the first methane-air non-reacting simulation at atmospheric pressure. The mesh dependence as well as an automatic refinement technique are also investigated. Thanks to this technique, the LES simulation was shown to well reproduce the inner and outer shear layers of the flow with a relatively low computational time.

The other cases correspond to CH_4/O_2 high pressure (60 bars) LES where experimental data are not available. First, the geometrical dimensions were fixed and some global parameters were estimated : burned gas properties (adiabatic temperature and density), the flame length using the model to be evaluated, the computational time as well as convective and radiative thermal fluxes.

For the second simulation, some instantaneous and time averaged fields were shown and the flame length obtained by the low order model was compared with that obtained by the numerical results. A difference of 3 % was obtained validating this low order model at high pressure in cold condition. Numerical result for the evolution of the methane mass fraction was also compared to an experimental scaling law from the literature. After introducing factors allowing to take into account the swirl effect and density difference in the scaling law, a very good agreement with the numerical results was found.

The third simulation were carried out in adiabatic reactive case where heat losses were not been considered. The temperature and mixture fraction fields were first analyzed. It was verified that the chemical time of such a reaction is very small and the effect of the combustor's walls confinement was noticed. As for the previous case, comparison between model and numerical flame length were made where only a difference of 10 % was found verifying the validity of this model in high-pressure oxy-combustion condition. A satisfying agreement was also when comparing with the scaling law by introducing the effect of the temperature increase on the density in this law.

The effects of heat losses are taken into account in the last isothermal simulation. It has been shown that these losses have a slight effect on the flame length. Finally, the radiative heat fluxes are calculated for one instantaneous solution. A high rate of absorption has been obtained. These heat losses were also compared to the estimations given by low order models presented before. Far agreement were found. For future studies, a coupling between the fluid dynamics and the radiative codes may be considered.

REFERENCES

[1] Kanniche, M., Gros-Bonnivard, R., Jaud, P., Valle-Marcos, J., Amann, J.-M., and Bouallou, C., 2010. "Pre-combustion, post-combustion and oxy-combustion in thermal power plant for co2 capture". *Applied Thermal Engineering,* ***30***(1), pp. 53–62.

[2] Normann, F., Andersson, K., Leckner, B., and Johnsson, F., 2008. "High-temperature reduction of nitrogen oxides in oxy-fuel combustion". *Fuel,* ***87***(17-18), pp. 3579–3585.

[3] Liu, C., Chen, G., Sipöcz, N., Assadi, M., and Bai, X.-S., 2012. "Characteristics of oxy-fuel combustion in gas turbines". *Applied Energy,* ***89***(1), pp. 387–394.

[4] Hong, J., Chaudhry, G., Brisson, J., Field, R., Gazzino, M., and Ghoniem, A. F., 2009. "Analysis of oxy-fuel combustion power cycle utilizing a pressurized coal combustor". *Energy,* ***34***(9), pp. 1332–1340.

[5] Gopan, A., Kumfer, B. M., Phillips, J., Thimsen, D., Smith, R., and Axelbaum, R. L., 2014. "Process design and performance analysis of a staged, pressurized oxy-combustion (spoc) power plant for carbon capture". *Applied Energy,* ***125***, pp. 179–188.

[6] Auchet, O., Riedinger, P., Malasse, O., and Iung, C., 2008. "First-principles simplified modelling of glass furnaces combustion chambers". *Control Engineering Practice,* ***16***(12), pp. 1443–1456.

[7] Förster, T., Voloshchuk, Y., Richter, A., and Meyer, B., 2017. "3d numerical study of the performance of different burner concepts for the high-pressure non-catalytic natural gas reforming based on the freiberg semi-industrial test facility hp pox". *Fuel,* ***203***, pp. 954–963.

[8] Sanz, W., Jericha, H., Bauer, B., and GÃķttlich, E., 2008. "Qualitative and quantitative comparison of two promising oxy-fuel power cycles for co2 capture". *Journal of Engineering for Gas Turbines and Power,* ***130***(3), p. 031702.

[9] Kim, H. K., Kim, Y., Lee, S. M., and Ahn, K. Y., 2006. "Emission characteristics of the 0.03 mw oxy- fuel combustor". *Energy & fuels,* ***20***(5), pp. 2125–2130.

[10] Sautet, J., Salentey, L., Ditaranto, M., and Samaniego, J., 2001. "Length of natural gas-oxygen non-premixed flames". *Combustion science and technology,* ***166***(1), pp. 131–150.

[11] Degenève, A., Vicquelin, R., Mirat, C., Labegorre, B., Jourdaine, P., Caudal, J., and Schuller, T., 2019. "Scaling relations for the length of coaxial oxy-flames with and without swirl". *Proceedings of the Combustion Institute,* ***37***(4), pp. 4563–4570.

[12] Peters, N., and Göttgens, J., 1991. "Scaling of buoyant turbulent jet diffusion flames". *Combustion and Flame,* ***85***(1-2), pp. 206–214.

[13] Villermaux, E., and Rehab, H., 2000. "Mixing in coaxial jets". *Journal of Fluid Mechanics,* ***425***, pp. 161–185.

[14] Schumaker, S. A., and Driscoll, J. F., 2009. "Coaxial turbulent jet flames: Scaling relations for measured stoichiometric mixing lengths". *Proceedings of the Combustion Institute,* ***32***(2), pp. 1655–1662.

[15] Merlo, N., Boushaki, T., Chauveau, C., De Persis, S., Pillier, L., Sarh, B., and Gökalp, I., 2014. "Combustion characteristics of methane–oxygen enhanced air turbulent non-

premixed swirling flames". *Experimental thermal and fluid science,* ***56***, pp. 53–60.

[16] Syred, N., Chigier, N., and Beer, J., 1971. "Flame stabilization in recirculation zones of jets with swirl". In Symposium (International) on Combustion, Vol. 13, Elsevier, pp. 617–624.

[17] Chen, R.-H., Driscoll, J. F., Kelly, J., Namazian, M., and Schefer, R., 1990. "A comparison of bluff-body and swirl-stabilized flames". *Combustion Science and Technology,* ***71***(4-6), pp. 197–217.

[18] Degeneve, A., Mirat, C., Caudal, J., Vicquelin, R., and Schuller, T., 2019. "Effects of swirl on the stabilization of non-premixed oxygen-enriched flames above coaxial injectors". *Journal of Engineering for Gas Turbines and Power,* ***141***(12).

[19] Tacina, K. M., and Dahm, W. J., 2000. "Effects of heat release on turbulent shear flows. part 1. a general equivalence principle for non-buoyant flows and its application to turbulent jet flames". *Journal of Fluid Mechanics,* ***415***, pp. 23–44.

[20] Seepana, S., and Jayanti, S., 2009. "Flame structure and no generation in oxy-fuel combustion at high pressures". *Energy Conversion and Management,* ***50***(4), pp. 1116–1123.

[21] Krieger, G., Campos, A., Takehara, M., Da Cunha, F. A., and Veras, C. G., 2015. "Numerical simulation of oxy-fuel combustion for gas turbine applications". *Applied Thermal Engineering,* ***78***, pp. 471–481.

[22] Colin, O., and Rudgyard, M., 2000. "Development of high-order taylor–galerkin schemes for les". *Journal of Computational Physics,* ***162***(2), pp. 338–371.

[23] Nicoud, F., Toda, H. B., Cabrit, O., Bose, S., and Lee, J., 2011. "Using singular values to build a subgrid-scale model for large eddy simulations". *Physics of Fluids,* ***23***(8), p. 085106.

[24] Poinsot, T. J., and Lelef, S., 1992. "Boundary conditions for direct simulations of compressible viscous flows". *Journal of computational physics,* ***101***(1), pp. 104–129.

[25] Pierce, C. D., and Moin, P., 2004. "Progress-variable approach for large-eddy simulation of non-premixed turbulent combustion". *Journal of fluid Mechanics,* ***504***, pp. 73–97.

[26] Fiorina, B., Vicquelin, R., Auzillon, P., Darabiha, N., Gicquel, O., and Veynante, D., 2010. "A filtered tabulated chemistry model for les of premixed combustion". *Combustion and Flame,* ***157***(3), pp. 465–475.

[27] Ihme, M., and Pitsch, H., 2008. "Prediction of extinction and reignition in nonpremixed turbulent flames using a flamelet/progress variable model: 2. application in les of sandia flames d and e". *Combustion and flame,* ***155***(1-2), pp. 90–107.

[28] CORDIER, M., BENARD, P., LYBAERT, P., and BRICTEUX, L. "Simulation aux grandes échelles de la flamme "jet-in-hot-coflow"".

[29] Tessé, L., Dupoirieux, F., Zamuner, B., and Taine, J., 2002. "Radiative transfer in real gases using reciprocal and forward monte carlo methods and a correlated-k approach". *International Journal of Heat and Mass Transfer,* ***45***(13), pp. 2797–2814.

[30] Goody, R., West, R., Chen, L., and Crisp, D., 1989. "The correlated-k method for radiation calculations in nonhomogeneous atmospheres". *Journal of Quantitative Spectroscopy and Radiative Transfer,* ***42***(6), pp. 539–550.

[31] Daviller, G., Brebion, M., Xavier, P., Staffelbach, G., Müller, J.-D., and Poinsot, T., 2017. "A mesh adaptation strategy to predict pressure losses in les of swirled flows". *Flow, Turbulence and Combustion,* ***99***(1), pp. 93–118.

[32] Richter, A., Seifert, P., Compart, F., Tischer, P., and Meyer, B., 2015. "A large-scale benchmark for the cfd modeling of non-catalytic reforming of natural gas based on the freiberg test plant hp pox". *Fuel,* ***152***, pp. 110–121.

[33] Dahm, W. J., 2005. "Effects of heat release on turbulent shear flows. part 2. turbulent mixing layers and the equivalence principle". *Journal of Fluid Mechanics,* ***540***, pp. 1–19.

[34] Yuen, W. W., 2008. "Definition and evaluation of mean beam lengths for applications in multidimensional radiative heat transfer: A mathematically self-consistent approach". *Journal of Heat Transfer,* ***130***(11), p. 114507.

[35] Lefebvre, A. H., and Herbert, M., 1960. "Heat-transfer processes in gas-turbine combustion chambers". *Proceedings of the institution of Mechanical Engineers,* ***174***(1), pp. 463–478.

[36] Rivière, P., and Soufiani, A., 2012. "Updated band model parameters for h2o, co2, ch4 and co radiation at high temperature". *International Journal of Heat and Mass Transfer,* ***55***(13-14), pp. 3349–3358.

[37] MANDELL, D. A., 1974. "Exact and mean beam length calculations for radiative heat transfer in gases". *Combustion Science and Technology,* ***9***(5-6), pp. 273–276.

[38] Edwards, D., and Balakrishnan, A., 1973. "Thermal radiation by combustion gases". *International Journal of Heat and Mass Transfer,* ***16***(1), pp. 25–40.

[39] Xuan, Y., and Li, Q., 2003. "Investigation on convective heat transfer and flow features of nanofluids". *Journal of Heat transfer,* ***125***(1), pp. 151–155.